Dynamic chemical expansion of thin-film non-stoichiometric oxides at extreme temperatures

Dynamic chemical expansion of thin film non-stoichiometric oxides at extreme temperatures

Jessica G. Swallow[1,2], Jae Jin Kim[1,2], John M. Maloney[1], Di Chen[1,2], James F. Smith[3], Sean R. Bishop[1,2], Harry L. Tuller[1,2], Krystyn J. Van Vliet[1,2,*]

[1] Department of Materials Science and Engineering, Massachusetts Institute of Technology, Cambridge, MA, 02139

[2] Materials Processing Center, Massachusetts Institute of Technology, Cambridge, MA, 02139

[3] Micro Materials Ltd., Wrexham, LL13 7YL, UK

* Corresponding Author. *Address:* Laboratory for Material Chemomechanics; Massachusetts Institute of Technology; 77 Massachusetts Avenue; Cambridge, MA, 02139

Email: krystyn@mit.edu

Abstract

Actuator operation in increasingly extreme and remote conditions requires materials that reliably sense and actuate at elevated temperatures, and over a range of gas environments. Design of such materials will rely on high-temperature, high-resolution approaches for characterizing material actuation *in situ*. Here, we demonstrate a novel type of high-temperature, low-voltage electromechanical oxide actuator based on the model material $Pr_xCe_{1-x}O_{2-\delta}$ (PCO). Chemical strain and interfacial stress resulted from electrochemically pumping oxygen into or out of PCO films, leading to measureable film volume changes due to chemical expansion. At 650°C, nanometer-scale displacement and strain of >0.1% were achieved with electrical bias values <0.1 V, low compared to piezoelectrically driven actuators, with strain amplified fivefold by stress-induced structural deflection. This *operando* measurement of films "breathing" at second-scale temporal resolution also enabled detailed identification of the controlling kinetics of this response, and can be extended to other electrochemomechanically coupled oxide films at extreme temperatures.

Materials that enable mechanical actuation and sensing in extreme environments are in high demand for applications including nuclear power control systems[1], jet turbine engines[2], and space exploration[3]. The artificial muscles required of these devices (e.g., electric motors and piezoelectrics) are often limited by material microstructural or compositional instability at high temperatures (>200°C).[4,5] Further, design of new materials to operate in such extreme environments is limited by lack of direct, high-temperature, high-resolution characterization of actuation. Here, we demonstrate the functionality of non-stoichiometric oxide thin films as a new class of high-temperature, non-volatile, and low-voltage electromechanical actuators, using $Pr_xCe_{1-x}O_{2-\delta}$ (PCO) as a model system. PCO, like many non-stoichiometric oxides, exhibits chemical expansion, or a coupling between material volume and composition, at temperatures >500°C that relate to elevated oxygen vacancy concentrations.[6] This oxide expansion at high temperatures can be enhanced at low oxygen partial pressures, or as demonstrated herein by electrochemical pumping in of oxygen vacancies with an applied electrical bias. For films adhered to substrates, the resulting chemically driven strain and associated interfacial stress can induce both volume change in the film and structural deflection of the system.

To quantify this film "breathing" and deflection due to reversible oxygen uptake within PCO thin films, we employed a distinct probe-based approach (Fig. 1) capable of nanometer-scale displacement and sub-second-scale temporal resolution at temperatures up to 650°C. In this method, a film of up to micrometer-scale thickness is electrically biased with modest voltages (~100 mV) to drive oxygen content changes within the entire film by adjusting the Nernst electrochemical potential.[7-9] An instrumented but nonconductive displacement probe placed in contact with the film concurrently measures the mechanical response to the applied bias. This approach has several key advantages over existing techniques to measure film expansion by

58 detecting changes in curvature[10], diffraction[11-15], volume[16], or scanning probe electrodes[17-19],
59 particularly at the high temperatures (well over 200°C) and low electrical biases (well below 1
60 V) of interest herein; see Supplementary Information (SI) Section 1. This decoupling of electrical
61 bias and mechanical displacement enabled demonstration of nanoscale electrochemomechanical
62 spectroscopy (NECS) on a model high-temperature oxide actuator under conditions characteristic
63 of extreme operating environments, to quantify mechanisms controlling the extent and rate of
64 device actuation.

65 The model film material of interest is $Pr_{0.1}Ce_{0.9}O_{2-\delta}$ (abbreviated as PCO, where δ
66 indicates non-stoichiometry), a functional oxide that exhibits large strain coupling to δ and has
67 been extensively characterized by a detailed defect model relating temperature and effective
68 pO_2.[8,16,20] In PCO, chemical expansion arises largely from an increase in ionic radius of cations
69 during the following reduction reaction, written using Kröger-Vink notation:[16,21]

(1) $$2Pr_{Ce}^{\times} + O_O^{\times} \leftrightarrow 2Pr_{Ce}^{'} + V_O^{\bullet\bullet} + \frac{1}{2}O_2(g)$$

70

71 where Pr^{x}_{Ce} and $Pr^{'}_{Ce}$ respectively denote Pr^{+4} and Pr^{+3} on Ce^{+4} sites, and O^{x}_{O} and $V_O^{\bullet\bullet}$
72 respectively denote an oxide ion (neutral with respect to the lattice) and an oxide ion vacancy
73 (double positively charged with respect to the lattice) at an oxygen site. We have demonstrated
74 previously that in thin films supported on ionically conducting substrates, this equilibrium can be
75 controlled both by changing the surrounding atmosphere and by application of electrical bias.[7,22]
76 The corresponding strain ε arising from the change in non-stoichiometry Δδ is analogous to
77 thermal expansion; this can be defined as:

(2) $$\varepsilon = \alpha_c \Delta\delta$$

where the unitless chemical expansion coefficient α_c is 0.087 for PCO.[16] Film adherence to the yttria-stabilized zirconia (YSZ) substrate constrains in-plane chemical strain to produce interfacial stress that can be sufficient to induce detectable deflection. Figure 1 summarizes the film configuration and measurement of NECS at constant elevated temperature. PCO films of varying thickness (~300 to 1000 nm) and approximately 8 x 8 mm in plane dimensions on YSZ single crystal substrates were fabricated with a three-electrode configuration (Fig. 1a; see Methods). Control samples lacking only the PCO film were also prepared to decouple the response of the film from that of the substrate and Pt electrodes, and one PCO/YSZ sample with smaller in-plane film dimensions (3 mm diameter) was prepared to decouple out-of-plane strain from deflection.

During mechanical measurements, a position-sensing probe was placed in contact with the film surface as a sinusoidal electrical bias was applied to the working electrode with respect to the reference electrode (Fig. 1b), and the mechanical displacement was detected as a combination of film thickness change and substrate deflection. Figure 1c shows example traces, illustrating that positive applied bias causes negative probe displacement as the film contracts, while a reduction in bias produces concomitant, reversible film expansion and positive probe displacement. This oxide film contraction under positive bias is expected from the higher effective oxygen partial pressure $pO_{2,eff}$ in the film given by the Nernst relation:

$$pO_{2,eff} = pO_{2,g} \exp[4qE/kT] \quad (3)$$

where E is the applied electrical bias. The asymmetry in magnitude of mechanical response apparent in Fig. 1c is also reasonably explained by the asymmetry in defect concentration change with respect to applied bias: PCO tends toward stoichiometry ($\delta \rightarrow 0$) under more oxidizing conditions and toward $\delta = 0.05$ for more reducing conditions. We detected such reversible,

nanometer-scale mechanical response, using electrical biasing frequencies ω ranging from 1 to 0.01 Hz. Probe displacement on film-free control samples exposed to oscillatory electrical bias was <1 nm; we thus concluded that there was little to no detectable contribution to the measured mechanical response from dimensional changes in the substrate, counter-electrode, or current collector. Curvature of the film/substrate system was detected by acquiring measurements at multiple surface locations with mm-scale lateral spacing relative to the film center; see SI Section 2, Fig. S1. Therefore, we attribute the dynamic actuation exemplified in Fig. 1b to concurrent increased PCO film thickness and positive substrate curvature due to interfacial stress.

The oscillatory mechanical response may be characterized by a phase lag ϕ and amplitude A by fitting a sinusoidal function to the probe position (Fig. 1c). Given sufficient time to relax following a change in oxygen activity, the sample can equilibrate fully. Accordingly, with decreasing frequency, the amplitude approaches a maximum value (~10 nm), whereas the phase lag approaches zero (Figs. 2a, b). Further, at higher temperatures with concurrent reduction in oxygen transport barriers, the frequency at which the maximum amplitude is reached increases. As mentioned above, we refer to this mechanical characterization of the sample frequency response as nanoscale electrochemomechanical spectroscopy (NECS), in analogy to electrical admittance spectroscopy, and determine the complex function Y describing the frequency response of the material relative to the applied signal. (See SI Section 4 for a detailed derivation of this transfer function.) The complex function Y can be described by its modulus A and phase lag ϕ using Eqs. 4-5, where τ is the characteristic time of the response and D_0 is the equilibrium displacement amplitude for each sample condition:[23]

(4) $$A = \frac{D_0}{\sqrt{(\omega\tau)^2 + 1}}$$

(5) $$\phi = -\varphi = \tan^{-1}(\omega\tau)$$

Figures 2a-b show that the measured deflection amplitudes and phase lags were well described by Eqs. 4-5, except at the highest frequencies (≥ 0.5 Hz) where phase lag is expected to asymptotically approach π/2 but exceeds this value experimentally. This discrepancy is explained by a slight internal signal collection delay (see SI Section 5). When these data are expressed on the complex plane for a given condition, as in Fig. 2c, the displayed NEC spectrum shows a single characteristic maximum (e.g., ~0.05 Hz at 650°C) corresponding to the characteristic frequency of the sample (where ωτ =1). As derived in SI Section 4, the arc diameter in Fig. 2c corresponds to the maximum mechanical displacement D_0, normalized by applied bias amplitude E_0, and τ/D_0 is the inverse rate of displacement. Note that the above relationships and following kinetics analysis are valid even for displacement attributed to concurrent film expansion and substrate curvature.

The capacity to rapidly measure these breathing displacements over a wide range of temperatures and bias-modulated defect contents enables determination of the activation energies E_a indicative of mechanisms by which oxygen moves in and out of functional oxides. Figure 3a shows representative Arrhenius relations from which the activation energies modulating the magnitude of mechanical response D_0 and inverse rate of expansion τ/D_0 for a given sample and condition were determined. These average E_a values were -1.05 ± 0.13 eV (for τ/D_0), and 0.53 ± 0.14 eV (for D_0), reported as mean and standard deviation of at least 6 measurements across 3 samples. We also applied conventional *in situ* impedance spectroscopy (IS) to these same sample constructs at 500-700°C, which allows for separate measurements of activation energies

145 associated with electrical impedance between different working electrodes. We thus determined
146 that the distinct activation energies measured mechanically were consistent with those
147 attributable specifically to the oxygen storage capacity, i.e., chemical capacitance, of the PCO
148 film (E_a measured by IS at 0.55 ± 0.07 eV corresponds to displacement magnitude D_0) and to
149 resistance to oxide ion conduction through the YSZ (E_a measured by IS at -0.99 ± 0.06 eV
150 corresponds to inverse displacement rate τ/D_0). These activation energies also agreed well with
151 those reported previously for PCO chemical capacitance [0.6 eV[24]] and YSZ diffusion (1 eV[25]).
152 In accordance with the derivations given for D_0 and τ/D_0 in SI, the good agreement with
153 expected activation energies validated that the calculated maximum breathing displacements D_0
154 of these oxide films are controlled by the chemical capacitance of the thin film PCO, and that the
155 inverse displacement rate τ/D_0 is controlled by the rate of oxygen transport into and out of the
156 PCO film through the YSZ substrate.

157 Figure 3b shows that D_0 was approximately linear with film thickness t_f, for different
158 temperatures and applied bias amplitudes, with a vertical intercept at $t_f = 0$ of $D_0 \sim \pm 1$ nm similar
159 to that detected for control samples (i.e., YSZ substrates with no PCO film). As expected,
160 displacement amplitude increased with increasing temperature at a given applied bias, e.g., up to
161 12 nm at 128 mV and 650°C for the 1018 nm film. Further, increasing the amplitude of the
162 applied bias from 128 to 171 mV (increasing effective pO_2 range by two orders of magnitude) at
163 a constant temperature of 650°C increased D_0 of that sample up to 16 nm. The observed
164 mechanical response to rapid changes in electrical bias indicates dimensional oscillation in the
165 PCO film that is driven by corresponding changes in oxide ion vacancy content.

166 To our knowledge, this is the first direct demonstration of such chemical-expansion-driven
167 actuation at high temperatures by oxide films, with tens of nm cyclic actuation at hundreds of

mV applied bias under sustained 650°C environments. Furthermore, the above measurements are consistent with expectations shown in Fig. 3c from the PCO defect model: PCO is expected to contract upon a combination of decreased oxide ion vacancy and Pr^{3+} ion concentrations (oxidizing condition, positive bias), and vice versa for increased oxide ion vacancy and Pr^{3+} ion concentrations (reducing condition, negative bias).[16,21] As the film is driven to expand in-plane, interfacial stress can drive substrate deflection at sufficient stress magnitudes and film lateral dimensions. Indeed, curvature was detectable (SI Section 2 and Fig. S1) for films of 8 mm in-plane dimensions as used in Figs. 1-4, while out-of-plane film expansion of ~1 nm, but not deflection, was detected for a PCO film of ~1 μm thickness but significantly smaller lateral dimensions at 650°C (SI Section 3 and Fig. S2). Negative substrate curvature amplifies displacement due to film contraction, while positive substrate curvature amplifies film expansion. The observed increases in D_0 caused by increased temperature or applied bias amplitude are also reasonable, in that these factors widen the equilibrium boundaries of accessed vacancy concentration and thus increase the mechanical response. Equilibrium or maximum actuation amplitude is thus proportional to film thickness.

We next consider how chemical strain produced in PCO films subjected to the conditions of this study relates to the displacement amplitude that was observed for all samples. Figure 3c shows that the expected equilibrium strain in these PCO films is 0.2 – 0.5% (see SI Section 6 for derivation) depending on applied bias and temperature; this estimate also includes a twofold increase in the strain of a constrained film as compared to a freestanding membrane.[7,16,22,26] Figure 3d shows that the detected displacement signal of these PCO-YSZ actuators was consistently amplified over the expected breathing strains as computed in Fig. 3c, by a factor of 5. This specific amplification factor is a function of the film lateral dimensions and substrate

thickness, and could therefore be tuned accordingly. Additionally, the significant actuation amplitude observed under such extreme environments is repeatable for many cycles and on different samples, and can be tuned further by adjusting film thickness, operating temperature, or applied bias range. The effect described herein for PCO films at temperatures above 500°C is distinct from the electrostrictive effect described by Lubomirsky et al. for Gd-doped cerium oxide (GDC) at temperatures below 200°C;[27,28] those effects in GDC rely on the ordering of vacancies that would not be present at such high temperature, would require much larger electric fields than applied in the present study, and would not be polarity dependent.

Figure 4 summarizes this approach and the findings for PCO films at elevated temperature and dynamically oscillated oxygen content, driven by oscillating anodic and cathodic bias. The approach directly measures displacement, rather than lattice parameter changes as would be characterized by diffraction, and can be adapted depending on sample design to detect stress-amplified actuation or pure film strain on the scale of nm, including at *operando* high temperatures and gas environments. NECS can also be used to estimate changes in activation energy and breathing mechanisms in these or other functional oxide films (e.g., battery cathode materials) and multilayers as a function of composition or extreme environment, including the potential for spatially resolved mapping (Figs. S1-2). NECS also provides quantitative insights into the dynamic mechanical response of such materials to electrochemical driving forces, and should facilitate new understanding of materials and conditions that maximize or minimize stress, strain, and fracture under redox cycling or gas interruption for applications in fuel cells, electrolyzers, catalysis, or gas sensors, or in response to electrical signals or environmental stimuli for sensor or actuator applications.

213 Beyond this general methodology to directly measure nanoscale actuation under
214 *operando* conditions, the electrochemically driven breathing response of these specific non-
215 stoichiometric oxide films presents advantages for high temperature actuation. For example, at a
216 given material thickness of 1 μm, the electrical bias required to produce 0.1% strain is effectively
217 reduced by three orders of magnitude for this PCO system as compared to state-of-the-art high
218 temperature piezoelectric materials[5] (see SI Section 7); additionally, this actuation is accessible
219 under sustained temperatures far exceeding those at which most piezoelectric actuators operate.
220 Similar to a piezoelectric, the strain response of our system is reversibly proportional to the
221 applied voltage, unlike other electrochemical devices that exhibit more step-wise behavior from
222 multiple redox reactions.[29] The PCO actuator described herein acts as a model system; there are
223 many chemomechanically coupled non-stoichiometric oxides that could operate according to the
224 same principles.[6,9,11] Furthermore, this design of such actuators has the advantage of non-volatile
225 mechanical memory: if leakage is sufficiently limited (e.g., by blocking gas exchange), the
226 device may be 'frozen' in place upon disconnection of the circuit that permits ionic mobility.
227 This opens up a new design space of high-temperature, low voltage micro-electromechanical
228 systems based on a mechanism that couples electrical signals to mechanical stress and strain via
229 material defect chemistry. Devices based on this alternative actuation mechanism are expected to
230 be of interest to the design of robotics in extreme environments ranging from nuclear power
231 plants to turbine engines to spacecraft.
232
233 **Methods**
234 Sample Fabrication:

235 Films of $Pr_{0.1}Ce_{0.9}O_{2-\delta}$ (PCO) with thicknesses of 371 ± 11, 600 ± 20, 883 ± 13, and 1018
236 ± 26 nm were grown by pulsed laser deposition (PLD) on single crystal (100) YSZ substrates
237 (MTI Corporation, Richmond, CA) of dimensions 10 x 10 x 1.0 mm^3. Substrates were heated to
238 500°C after reaching a base pressure of 8.5 x 10^{-6} torr, and a dense PCO target was ablated by
239 using a 248 nm wavelength coherent COMPex Pro 205 KrF eximer laser (Santa Clara, CA) with
240 an 8 Hz laser repetition rate at 400 mJ/pulse. An oxygen partial pressure of 10 mTorr was
241 maintained during both the deposition and cooling steps (5°C/min). Post-annealing with a sudden
242 increase in oxygen partial pressure at the deposition temperature in the PLD chamber was not
243 included to avoid severe cracks and delamination caused by rapid changes in film volume.
244 Except in the case of the 600 nm film which was measured by profilometry, film thickness was
245 measured by scanning electron microscopy of films that were cross-sectioned either by cleaving
246 or focused ion beam (FIB) milling (Helios Nanolab 600 Dual Beam Focused Ion Beam Milling
247 System, FEI, Burlington, MA). Film crystallographic texture was confirmed by X-ray diffraction
248 (X'Pert Pro MPD PANalytical diffractometer) from 2θ-ω coupled scans of the films, which
249 indicated a highly oriented (100) texture. Film surface roughness (root mean square) and grain
250 size were 1.3 ± 0.2 nm and 20 – 30 nm, respectively, obtained by atomic force microscopy
251 (Digital Instruments Nanoscope IV, Veeco, Plainview, NY).[30] Figures S5 and S6 in SI Section 8
252 provide representative examples of surface roughness and X-ray diffraction data.
253 Porous Pt layers, as the current collector for the PCO working electrode and as the
254 counter electrode were prepared by a combination of Pt paste and reactive sputtering on the PCO
255 film and the opposite PCO-free substrate surface, with thicknesses of 83 ± 4 nm and 159 ± 31
256 nm, respectively (as shown in Figure 1a). As described in detail previously, PtO_x thin films were
257 first prepared by reactive magnetron sputtering (Kurt J. Lesker, Clairton, PA) at a DC power of

50 W from a two-inch-diameter metal target of 99.99% Pt (ACI Alloys, San Jose, CA) under controlled argon/oxygen (3/7) atmosphere.[31] Pt paste was applied on the top of the sputtered PtO_x layer except in the center area of the PCO working electrode, which was reserved for the mechanical response measurements (i.e., the region where the probe tip rested on the film surface). Pt paste was also applied to the outer perimeter of the YSZ substrate to serve as the reference electrode. Then, the samples were annealed at 750°C in air for 2 hrs with a heating and cooling rate of 2°C/min. During this annealing step, PtO_x was reduced to Pt, resulting in a porous film structure. The sputtered porous Pt layer was used to provide a thin layer with controlled thickness in the area for the mechanical measurement in addition to enhancing adhesion between the Pt paste and ceramic surfaces. There was no evidence of film delamination, as confirmed by subsequent FIB milling to expose the film/electrolyte interfaces for all samples investigated in this study.

Nanoscale Electrochemomechanical Spectroscopy Measurement:

Samples were mounted onto a hot stage by applying high temperature cement (Omega-bond 600) to the corners of the sample leaving a gap for gas flow to the counterelectrode. Samples were heated at a rate of 1.6°C/min to temperatures 550, 575, 600, 625, and 650°C and allowed to reach equilibrium for at least 1 hour prior to testing. Samples were then brought into contact with a Berkovich-geometry, cubic boron nitride high-temperature probe using a MicroMaterials NanoTest Vantage instrumented indenter. Information on the stability of the cBN probe material and the precision of the NanoTest Vantage instrumented indenter is available in Section 10 of the Supplementary Information. Using the ModuLab system (Solartron Analytical, Oak Ridge, TN) in conjunction with the Potentiostat (PSTAT 1Ms/s) and Frequency

Response Analyzer (FRA 1MHz) module, sinusoidal electrical bias signals with amplitudes of 86, 128, and 171 mV were applied to the working electrode with respect to the reference electrode at frequencies of 0.01, 0.025, 0.05, 0.1, 0.25, 0.5, and 1Hz. The mechanical response of the sample was measured by displacement of the probe detected by the instrumented indenter resting on the sample surface, with the minimum mechanical load necessary to maintain contact. Each driving frequency was run for a minimum of 35 periods to ensure that the fitting algorithm described in SI Section 9 had measured the parameters of the response signal to suitable accuracy. Detailed discussion of the sensitivity of detected amplitudes and phase lags to experimental variation is available in SI Section 9.

Impedance Testing:

The asymmetrical cells used for the mechanical measurement as illustrated in Figure 1a were also investigated by electrochemical impedance spectroscopy (EIS). The EIS measurements were conducted at temperatures between 500°C and 700°C in air and covered the frequency range from ~1 – 10 mHz to 1 MHz with an AC amplitude of 20 mV and no DC bias using the ModuLab system (Solartron Analytical) described above. The electrode impedance of both the PCO working electrode and the Pt counter electrode were separately investigated by using a three-electrode cell configuration including a reference electrode. ZView software (Scribner Associates) was used to fit and construct equivalent circuits to analyze the results. The equivalent circuit models used to analyze these samples have been validated previously on PCO/YSZ systems of the same configuration.[22]

In addition to the activation energies reported above, impedance spectroscopy also showed that the PCO oxygen gas surface exchange reaction exhibited a considerably higher E_a of

304 2.22 ± 0.30 eV, and that the area specific resistance at the counter electrode exhibited E_a = 1.61 ±
305 0.11 eV.
306
307 Data Processing and Analysis:
308 Input (driving) and output (displacement) signals were collected by USB-6009 DAQ
309 (National Instruments) and a moving average across each driving cycle was subtracted to remove
310 background noise.[32] Each of the two flattened signals was then fitted by linear least squares to a
311 sum of sine and cosine waves as described in SI Section 9 to estimate the amplitude and phase
312 lag of the displacement signal relative to the input signal (V_{input} = A sin ωt + B cos ωt, V_{output} = C
313 sin ωt + D cos ωt where ω is the known driving frequency).[33] At each experimental condition,
314 oscillatory biasing (with real-time analysis) was conducted until the phase lag converged to
315 within 0.1 radians and the amplitude to within 0.5 nm, typically exceeding 30 cycles.
316 The measured phase lag ϕ and amplitude A of the final 10 cycles of data were averaged
317 for each frequency, and for a given condition (i.e., temperature and applied bias) the ϕ vs.
318 angular frequency ω relationship was fit to Equation 5 with one time constant τ that was then
319 used to fit the A vs. ω results to Eq. 4 to determine an equilibrium amplitude D_0 at maximum
320 applied bias. The fit was performed using customized Matlab software. These D_0 and τ values
321 were then used to estimate activation energies for the expansion signal as shown in Figure 3a,
322 and the fitted value of D_0 was used to estimate equilibrium (zero frequency) mechanical response
323 and determine the amplification factor. Reported activation energies are the average and standard
324 deviation of at least 6 measurements across all three samples tested. Detailed discussion of the
325 sensitivity of calculated D_0, τ, E_a, and amplification factor values to experimental and sample-to-
326 sample variation is available in SI Section 9.

Data Availability

Source data for Figures 1-3 and example film displacement data are available from the online data repository Figshare with identifier DOI:10.6084/m9.figshare.4681324. Remaining data that support the findings of this study are available from the corresponding author upon reasonable request.

References

1. Gelhaus, F. E. & Roman, H. T. Robot applications in nuclear power plants. *Progress in Nuclear Energy* **23,** 1–33 (1990).
2. Amrhein, M., Wells, J. & Baudendistel, T. Design of a high-temperature utility electromechanical actuator. *SAE Technical Paper* DOI:10.4271/2012-01-2214 (2012).
3. Sherrit, S. Smart material/actuator needs in extreme environments in space. *Proceedings of the SPIE Smart Structures and Materials Conference* **5761,** (2005).
4. Damjanovic, D. Materials for high temperature piezoelectric transducers. *Current Opinion in Solid State & Materials Science* **3,** 469–473 (1998).
5. Zhang, S. & Yu, F. Piezoelectric Materials for High Temperature Sensors. *J. Am. Ceram. Soc.* **94,** 3153–3170 (2011).
6. Bishop, S. R. *et al.* Chemical expansion: Implications for electrochemical energy storage and conversion devices. *Annu. Rev. Mater. Res.* **44,** 205–239 (2014).
7. Chen, D. & Tuller, H. L. Voltage-controlled nonstoichiometry in oxide thin films: $Pr_{0.1}Ce_{0.9}O_{2-\delta}$ case study. *Adv. Funct. Mater.* **24,** 7638–7644 (2014).
8. Bishop, S. R., Stefanik, T. S. & Tuller, H. L. Electrical conductivity and defect equilibria

of $Pr_{0.1}Ce_{0.9}O_{2-\delta}$. *Phys. Chem. Chem. Phys.* **13,** 10165–10173 (2011).

9. Lu, Q. & Yildiz, B. Voltage-controlled topotactic phase transition in thin-film $SrCoO_x$ monitored by in situ X-ray diffraction. *Nano Lett.* **16,** 1186–1193 (2016).

10. Sheldon, B. W., Mandowara, S. & Rankin, J. Grain boundary induced compositional stress in nanocrystalline ceria films. *Solid State Ionics* **233,** 38–46 (2013).

11. Hopper, E. M. *et al.* Oxygen exchange in $La_{0.6}Sr_{0.4}Co_{0.2}Fe_{0.8}O_{3-\delta}$ thin-film heterostructures under applied electric potential. *J. Phys. Chem. C* **119,** 19915–19921 (2015).

12. Hiraiwa, C. *et al.* Chemical expansion and change in lattice constant of Y-doped $BaZrO_3$ by hydration/dehydration reaction and final heat-treating temperature. *J. Am. Ceram. Soc.* **96,** 879–884 (2013).

13. Grande, T., Tolchard, J. R. & Selbach, S. M. Anisotropic thermal and chemical expansion in Sr-substituted $LaMnO_{3+\delta}$: Implications for chemical strain relaxation. *Chem. Mater.* **24,** 338–345 (2012).

14. Tomkiewicz, A. C., Tamimi, M. A., Huq, A. & McIntosh, S. Evidence for the low oxygen stoichiometry of cubic $Ba_{0.5}Sr_{0.5}Co_{0.5}Fe_{0.5}O_{3-\delta}$ from in-situ neutron diffraction. *Solid State Ionics* **253,** 27–31 (2013).

15. McIntosh, S., Vente, J. F., Haije, W. G., Blank, D. H. A. & Bouwmeester, H. J. M. Oxygen stoichiometry and chemical expansion of $Ba_{0.5}Sr_{0.5}Co_{0.8}Fe_{0.2}O_{3-\delta}$ measured by in situ neutron diffraction. *Chem. Mater.* **18,** 2187–2193 (2006).

16. Bishop, S. R., Tuller, H. L., Kuru, Y. & Yildiz, B. Chemical expansion of nonstoichiometric $Pr_{0.1}Ce_{0.9}O_{2-\delta}$: Correlation with defect equilibrium model. *J. Eur. Ceram. Soc.* **31,** 2351–2356 (2011).

17. Kalinin, S. V. & Balke, N. Local electrochemical functionality in energy storage materials

and devices by scanning probe microscopies: Status and perspectives. *Adv. Mater.* **22,** E193–E209 (2010).

18. Kumar, A., Ciucci, F., Morozovska, A. N., Kalinin, S. V. & Jesse, S. Measuring oxygen reduction/evolution reactions on the nanoscale. *Nature Chem.* **3,** 707–713 (2011).

19. Balke, N. *et al.* Nanoscale mapping of ion diffusion in a lithium-ion battery cathode. *Nature Nanotech.* **5,** 749–754 (2010).

20. Bishop, S. R., Stefanik, T. S. & Tuller, H. L. Defects and transport in $Pr_xCe_{1-x}O_{2-\delta}$: Composition trends. *J. Mater. Res.* **27,** 2009–2016 (2012).

21. Marrocchelli, D., Bishop, S. R., Tuller, H. L. & Yildiz, B. Understanding chemical expansion in non-stoichiometric oxides: Ceria and zirconia case studies. *Adv. Funct. Mater.* **22,** 1958–1965 (2012).

22. Chen, D., Bishop, S. R. & Tuller, H. L. Non-stoichiometry in oxide thin films: A chemical capacitance study of the praseodymium-cerium oxide system. *Adv. Funct. Mater.* **23,** 2168–2174 (2013).

23. Seborg, D. E., Edgar, T. F., Mellichamp, D. A. & Doyle, F. J., III. *Process Dynamics and Control*. (John Wiley & Sons, 2011).

24. Di Chen. Characterization and control of non-stoichiometry in $Pr_{0.1}Ce_{0.9}O_{2-\delta}$ thin films: Correlation with SOFC electrode performance. (PhD Thesis, Massachusetts Institute of Technology, 2014).

25. Manning, P. S., Sirman, J. D. & Kilner, J. A. Oxygen self-diffusion and surface exchange studies of oxide electrolytes having the fluorite structure. *Solid State Ionics* **93,** 125–132 (1997).

26. Bishop, S. R. *et al.* Impact of size scale on electro-chemo-mechanical coupling properties

in MIECs: Bulk and thin film (Pr,Ce)$O_{2-\delta}$. *ECS Trans.* **61,** 31–36 (2014).

27. Korobko, R. *et al.* Giant electrostriction in Gd-doped ceria. *Adv. Mater.* **24,** 5857–5861 (2012).

28. Korobko, R. *et al.* In-situ extended X-ray absorption fine structure study of electrostriction in Gd doped ceria. *Appl. Phys. Lett.* **106,** 042904 (2015).

29. Cheng, C. & Ngan, A. H. W. Reversible electrochemical actuation of metallic nanohoneycombs induced by pseudocapacitive redox processes. *ACS Nano* **9,** 3984–3995 (2015).

30. Kim, J. J., Bishop, S. R., Thompson, N., Kuru, Y., and Tuller, H. L. Optically derived energy band gap states of Pr in ceria. *Solid State Ionics* **225**, 198-200 (2012).

31. Jung, W., Kim, J. J. & Tuller, H. L. Investigation of nanoporous platinum thin films fabricated by reactive sputtering: Application as micro-SOFC electrode. *J. Power Sources* **275,** 860–865 (2015).

32. Maloney, J. M., Lehnhardt, E., Long, A. F. & Van Vliet, K. J. Mechanical fluidity of fully suspended biological cells. *Biophys. J.* **105,** 1767–1777 (2013).

33. Kutner, M. H., Nachtsheim, C. J., Neter, J. & Li, W. *Applied Linear Statistical Models*. (McGraw-Hill, Boston, 2005).

Acknowledgements

This work was supported by the U.S. Department of Energy, Basic Energy Sciences, Division of Materials Science and Engineering under award number DE-SC0002633. J. G. Swallow acknowledges support from the DOE-SCGF Fellowship Program administered by ORISE-ORAU under contract no. DE-AC05-06OR23100. J.J. Kim thanks the Kwanjeong Educational

Foundation for fellowship support. The authors acknowledge C.S. Kim for additional sample preparation and F. Frankel for assistance with figure preparation. This work made use of the Shared Experimental Facilities supported in part by the MRSEC Program of the National Science Foundation under award number DMR-1419807.

Author Contributions

JGS, JJK, HLT, and KJVV designed the study. JGS developed the dynamic expansion measurement technique and conducted displacement measurements and data analysis. JJK deposited films, conducted structural characterization and imaging, and impedance measurements. SRB developed analysis methods and relationships between impedance and mechanical results. JMM designed LabView signal analysis code for detecting expansion phase lag and amplitude. DC contributed to sample design and application of the defect model. JFS contributed to frequency-based measurement experimental design. JGS, JJK, SRB, HLT, and KJVV wrote the manuscript.

Additional Information

Supplementary information is available in the online version of the paper.

Competing Financial Interests

The authors declare no competing financial interests

Figure Legends

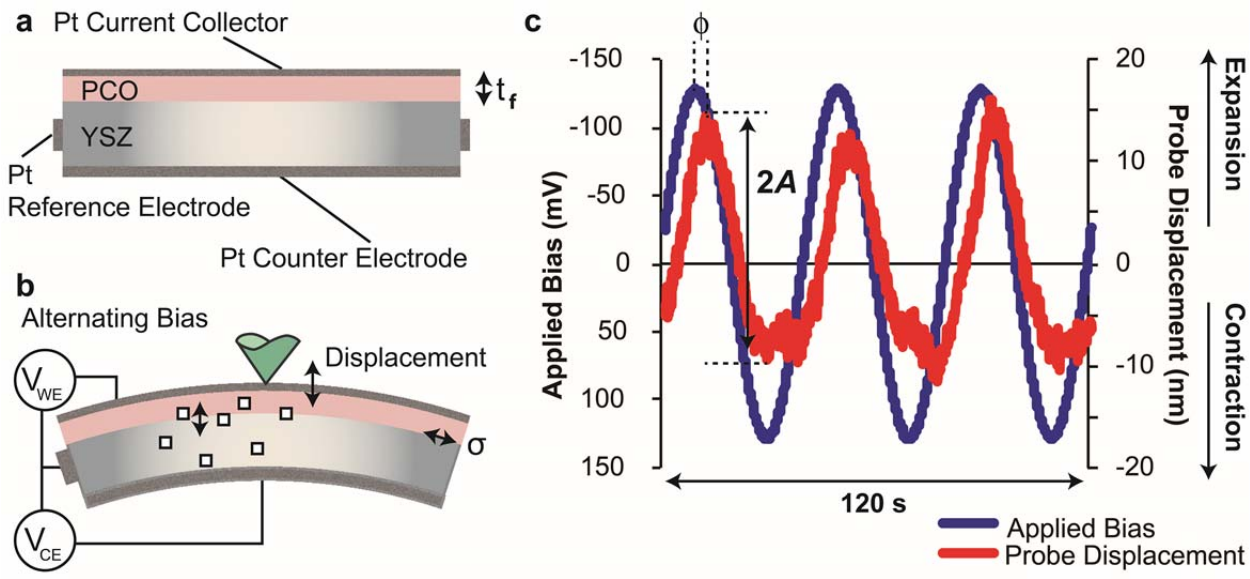

Figure 1. Dynamic chemical expansion upon oscillating electrical bias. (a) Films of $Pr_{0.1}Ce_{0.9}O_{2-\delta}$ (PCO) with deposited thickness t_f ranging from 300-1000 nm were grown on yttria stabilized zirconia (YSZ) single crystal substrates (1 mm thickness) with porous Pt reference and counter electrodes. (b) The depth-sensing probe rests in contact with the PCO sample surface, with the sample maintained at a constant temperature ranging from 550 to 650°C. Alternating bias V_{WE} applied to the working electrode with respect to the reference electrode modulates the oxygen activity in the PCO film, causing oxygen vacancies (empty squares) to be pumped in and out of the film through the YSZ substrate. This in turn leads to mechanical response that is the result of a combination of film volume change and substrate deflection due to PCO chemical expansion, detectable through probe displacement. (c) Sinusoidal applied bias (blue) induces a corresponding and lagging change in probe position (red), from which phase lag ϕ and amplitude *A* are detected. Positive probe displacement indicates increased film thickness (expansion) and positive substrate curvature and is driven by negative (reducing) bias, whereas negative displacement indicates decreased film thickness (contraction) and negative substrate curvature that is driven by positive (oxidizing) bias.

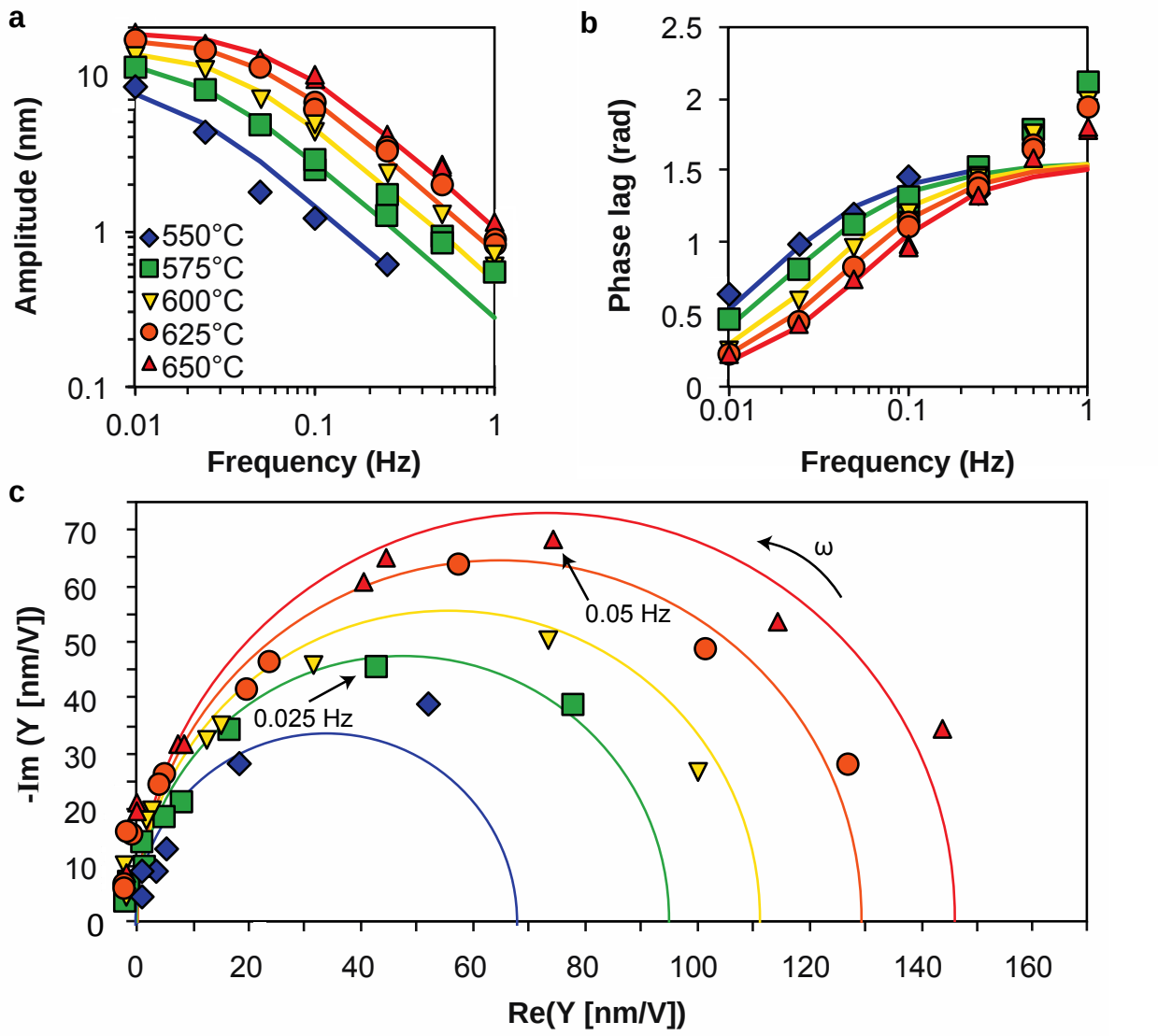

Figure 2. Sample frequency response to expanding $Pr_{0.1}Ce_{0.9}O_{2-\delta}$ film. Amplitude A (a) and phase lag ϕ (b) obtained at several different temperatures for PCO film thickness of 1 μm. For each temperature, A and ϕ are fit to a first-order transfer function (solid lines) to estimate the characteristic time τ and equilibrium (zero-frequency) displacement amplitude D_0 of the mechanical response. With increasing temperature, the expansion response is more rapid, suggesting a temperature-activated process. The discrepancy at higher frequencies between predicted and experimentally obtained phase lag values is discussed in SI Section 5. (c) Electrochemomechanical admittance Y shown on the complex plane for the same data indicates a

single semicircle or process at each temperature. In analogy to electrical admittance spectroscopy, corresponding diameters are equivalent to D_0/E_0, while the frequency at the semicircle maximum marks $\omega\tau = 1$. For all data points, the standard deviation of fitted A or ϕ over ten periods is smaller than the data points.

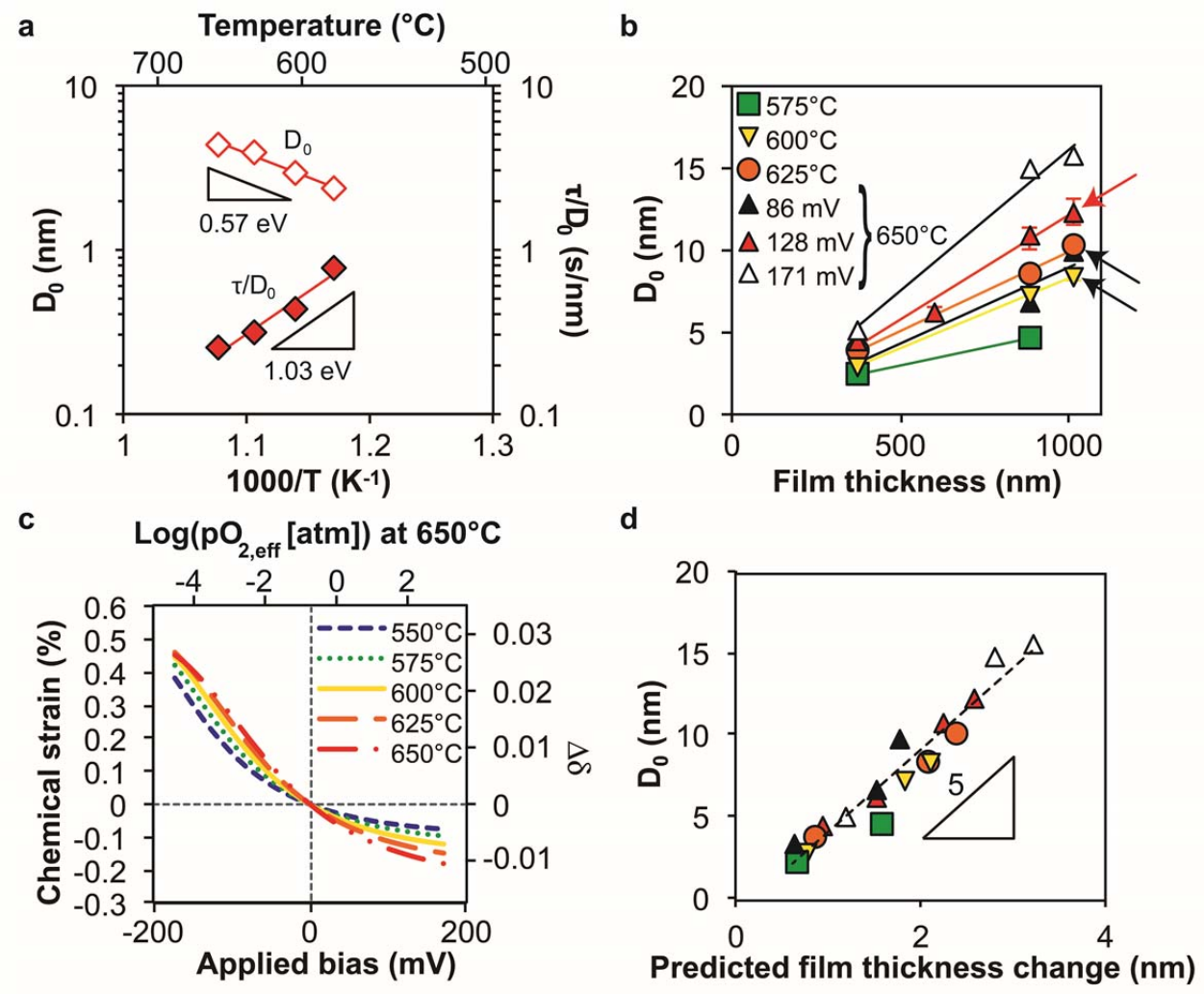

Figure 3. Factors controlling oxide film breathing. (a) Representative Arrhenius plots used to estimate the activation energy for YSZ diffusion and PCO chemical capacitance based on the values of τ/D_0 (inverse deflection rate) and D_0 (deflection magnitude), respectively, identified from the mechanical measurements. These activation energies are comparable to those calculated based on *in situ* impedance spectroscopy. Data shown are for PCO film thickness 371 ± 11 nm. (b) Equilibrium magnitude D_0 of probe displacement increases with increasing temperature, applied bias amplitude E_0, and film thickness. Data correspond to E_0 of 128 mV unless otherwise noted. Where possible, error bars show the range of measured D_0 values for three replicate measurements (All films at E_0 = 128 mV and T = 650 °C, highlighted by a red arrow, and all

temperatures with E_0 = 128 mV for the film with thickness 1018±26 nm, highlighted by black arrows). This range is often smaller than the size of the data points. (c) Out-of-plane strain ε and non-stoichiometry change Δδ vs. applied bias at several temperatures for a constrained PCO thin film as predicted by the defect model for $Pr_{0.1}Ce_{0.9}O_{2-\delta}$.[8,16,20] (d) Measured deflection amplitude D_0 vs. predicted film thickness change based on chemical strains calculated in (c) for the set of measurements shown in (b). A consistent amplification of 5 ± 0.5 nm/nm ($\Delta D_0/\Delta\varepsilon$) is observed across all samples, temperatures, and E_0 values, with error determined by bootstrapping as described in SI Section 9.

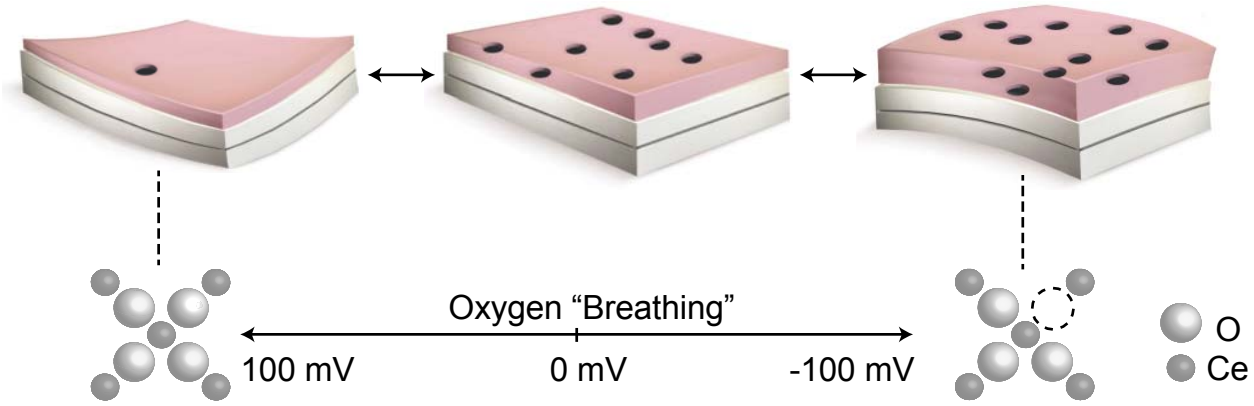

493

494 **Figure 4. Schematic of processes occurring during direct chemical expansion measurement**.
495 The film (pink) on an oxide ion conducting substrate (white) is biased with respect to the
496 reference electrode (gray circumscribed perimeter), oscillating between cathodic (negative,
497 reducing) and anodic (positive, oxidizing) conditions. Under anodic bias, the film breathes
498 oxygen in, producing an overall contraction and reduction in film thickness and corresponding
499 negative substrate deflection. Under cathodic bias, oxygen is released from the film, resulting in
500 increased oxide ion vacancy content (dark holes) and a corresponding increase in film thickness
501 and positive substrate deflection.

502

Supplementary Information: Dynamic chemical expansion of thin film non-stoichiometric oxides at extreme temperatures

Jessica G. Swallow, Jae Jin Kim, John M. Maloney, Di Chen, James F. Smith, Sean R. Bishop, Harry L. Tuller, and Krystyn J. Van Vliet

SI Contents:

1. Discussion of nanoscale electrochemomechanical spectroscopy as compared to prior methods of local or global material expansion measurements

The method described in the manuscript to measure film expansion and deflection *operando*, nanoscale electrochemomechanical spectroscopy (NECS), has several advantages over other reported methods to detect local or global material expansion and displacement. Specifically to oxides that exhibit this expansion due to reversible "breathing" of oxygen into the material, NECS can be conducted at controlled, elevated temperatures, under controlled gas environments, and with applied electrical biases to both modulate sample oxygen content and/or shift to non-stoichiometry conditions that are very difficult to access with oxygen partial pressure alone. NECS can also handle many different sample designs, including multilayer samples and samples with complex morphologies. It can be applied to laterally map sample deformation at different positions along a sample surface separated by only hundreds of nanometers, of interest for developing novel device structures. Additionally, NECS can be used to find conditions or materials that maximize or minimize chemical expansion effects under *in situ* conditions of temperature or defect content.

NECS is also distinct from other methods of measuring chemical expansion effects, in that it is more versatile and accessible than any one alternative approach. These methods include optical approaches (e.g., interferometry[1] or multi-beam optical stress sensors[2]), diffraction-based methods based on x-rays[3-5] or neutrons[6,7], and contact-based methods such as dilatometry[8] and scanning probe-based spectroscopy[9-11] methods that utilize the probe as an electrode.

Unlike curvature-based methods, NECS can be applied to measure both strain-only displacement and displacements amplified by substrate deflection. Further, unlike interferometry-based measurements, this method requires no particular knowledge of the optical properties of samples,

nor does it require samples to have specific optical properties (e.g., reflectivity) as are required for many curvature-based techniques. Unlike diffraction-based chemical expansion measurements, this method can measure displacements and volumetric expansion resulting from mechanisms other than lattice strain (e.g., that due to grain boundary mediated effects). Additionally, NECS can achieve second-scale temporal resolution for lattice-strain-based displacements without the aid of a synchrotron used in XRD or neutron diffraction (methods that can also include potentially damaging high energy radiation), and may be able to achieve faster temporal resolutions with additional modification of instrumentation and software. Unlike dilatometry, this method can be applied to thin film samples such as those discussed in the manuscript, and has improved spatial resolution as compared to most dilatometers.

Previous investigations of electrochemomechanical coupling in oxide bulk or thin films have employed scanning probe microscopy with nanoscale resolution.[9] While such electrochemical strain microscopy (ESM), as described by Kalinin et al., has enabled derivation of diffusion coefficients in cathode materials and provided insights into surface oxidation and evolution reactions, that approach employs the nanoscale probe tip itself as a moving electrode. As such, results reflect properties limited to regions within ~20 nm of the surface and due to the local perturbation near the nanoscale probe electrode.[10,11] Extension of that local biasing capability to the approach described in the present manuscript provides an important avenue for future work that compares global to local electrochemomechanical responses. However, at present such ESM investigations are limited generally to temperatures <200°C, and thereby requiring large electrical biases (>2 V) to obtain measurable displacement in response to polarization. The

resulting mechanisms under exploration are thus also specific to the combination of probe and sample materials.

As with any experimental method, there exist some limitations to the NECS method implemented in this study; these are described here. First, using NECS to acquire deflection-based measurements of quantitative chemical expansion (film strain as a function of applied bias) requires calibration of the relevant amplification factor for the sample geometry of interest. We suggest that PCO is an excellent model material for this purpose, due to the availability of accurate chemical expansion models for this material. For the geometry and attachment method of samples observed in this study (1 mm substrate thickness, 0.8x0.8 cm^2 film area) substrate deflection amplified the displacement signal by a factor of 5 relative to film thickness change alone, as highlighted in Figure 3d. The choice of electrode metal limits the temperature range for this method. For example, the use of silver paste to attach Pt wire to Pt electrodes set the maximum temperature for this study at ~650°C. An alternative choice could raise that temperature. Additionally, samples that have very fast surface oxygen exchange may experience oxygen leakage competing with electrochemical pumping; suggestions for mitigating this include use of blocking electrodes and designing samples where oxygen pumping is fast enough to overcome this limitation (e.g., by thinning the oxide ion conducting substrate).

2. Confirmation of sample deflection through detection of curvature

To confirm that samples were deflecting in response to applied electrical bias, a sample with the surface geometry shown in Figure S1a was tested at positions near and far from the center or the

clamped sample edges (as marked in the Figure). For each test, an oscillating bias of ±128 mV was applied for a frequency range of 1-0.025 Hz, and values of D_0 and τ were determined according to the model and fitting procedure outlined in Section 4 below and in the text. Figures S1b-c plot the results of this fit versus lateral probe position. D_0 is about a factor of 6 higher in the center than near the sample edges despite no apparent trend in the time constant τ; this indicates sample curvature during the measurement and confirms that the substrate is deflected as the film responds to the applied bias.

As a coarse estimate of expected deflection at the sample center, Stoney's formula predicts a D_0 of 42 nm for a PCO film of 600 nm thickness at 650°C subjected to chemical strain amplitude of 0.13% leading to interfacial stress amplitude estimated at 0.29 GPa.[12] This estimate is based on the following assumed elastic properties for YSZ and PCO: Young's modulus E_{PCO} = 150 GPa[13], Poisson's ratio ν_{PCO} = 0.33[14], E_{YSZ} = 272 GPa[15], ν_{YSZ} = 0.3[16]. The difference from the actually measured D_0 of 7 nm is explained by the fact that the assumptions of the boundary conditions of Stoney's formula are not accurately met by this experimental design (e.g., the sample is mounted to the heated stage with cement, the film only covers 64% of the substrate area).

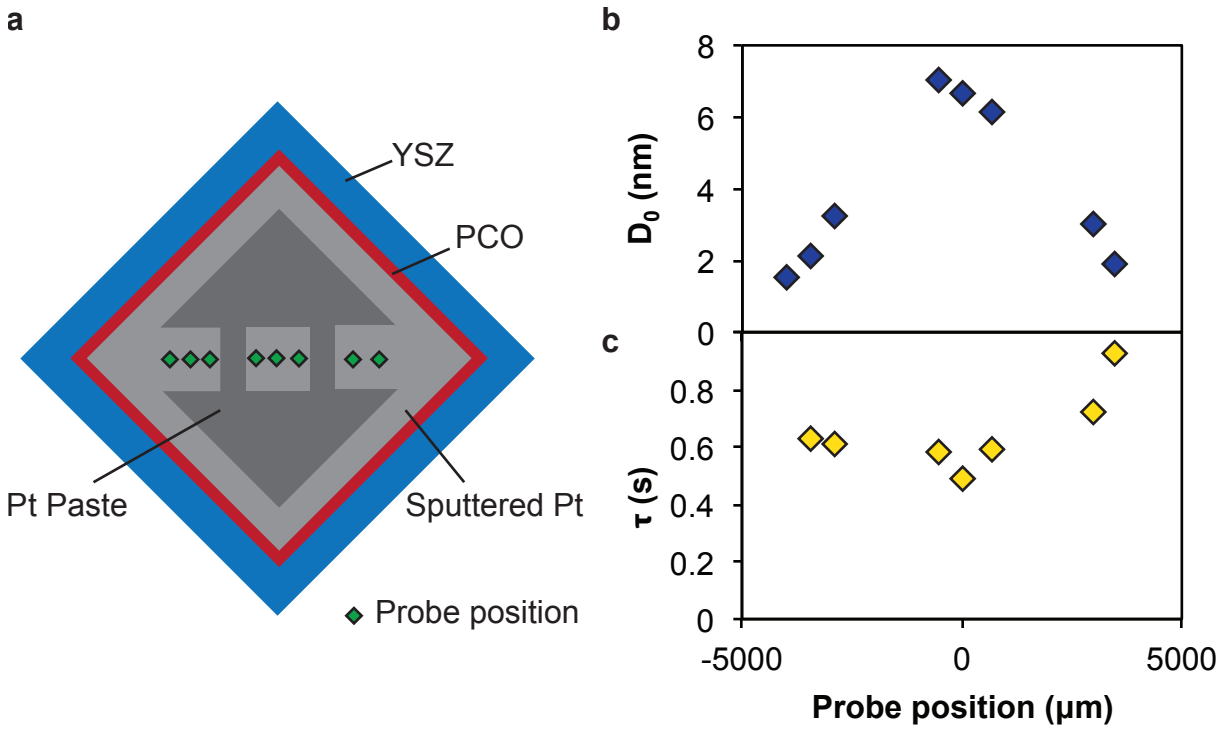

Figure S1. Samples deflect in response to applied bias. (a) Schematic of sample geometry and probe positions for testing deflection amplitude vs. position across the sample surface. A 600 nm film of $Pr_xCe_{1-x}O_{2-\delta}$ (PCO) was grown on a 1 mm-thick yttria stabilized zirconia (YSZ) substrate. The surface electrode is a sputtered layer of porous Pt. Pt paste was also added to improve connectivity of the surface electrode in regions where probe contact would not be necessary. Probe contact positions are not to scale. (b) Equilibrium deflection amplitude D_0 and (c) characteristic time constant τ vs. lateral probe position, indicating increased deflection near sample center as compared to sample edges confirms curvature upon application of electrical bias signal. The time constant is unaffected by probe position, as deflection rate is controlled by oxide ion diffusion through the substrate.

3. Measurement of strain-only displacement

To confirm that we could measure displacements resulting from chemical strain alone, we designed a sample to minimize substrate deflection by using a thick substrate (1.5 mm) and small film footprint (3 mm diameter, ~1 μm thickness as measured by profilometry). This prevented the film from developing enough interfacial stress under electrical-bias-stimulated chemical

expansion to induce substrate deflection. Figure S2 shows that 1 nm of displacement amplitude was measured consistently across the width of the film, with no sign of curvature due to substrate deflection. The measured displacement is therefore attributed solely to PCO film thickness change, confirming that the method described in this work for detecting dynamic chemical expansion can be applied to measure film thickness changes as well as displacements resulting from combined film thickness change and substrate deflection.

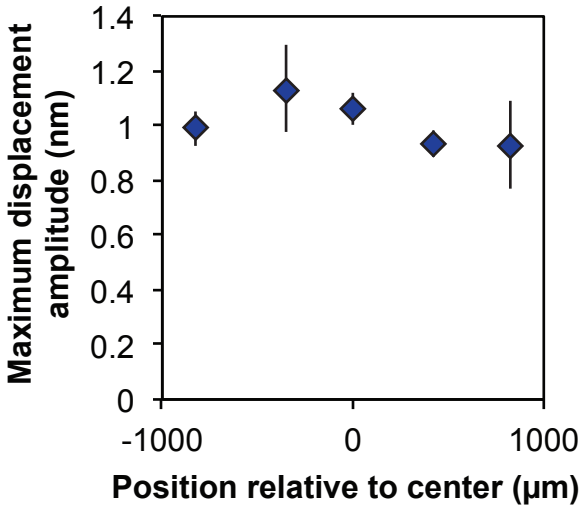

Figure S2. The measured displacement amplitude for a ~1 μm film with reduced area (3 mm diameter) grown on a 1.5 mm-thick substrate is consistently 1 nm across the width of the film, indicating the absence of substrate deflection under electrically stimulated chemical expansion. The measured displacement is therefore attributed solely to PCO film thickness change, confirming that this method can be used to detect chemical strains as small as 1 nm.

4. Frequency-response data plotted on the complex plane and discussion of electrochemomechanical admittance

Figures 2a and b from the manuscript present frequency response results of the films using Bode plots, showing directly amplitude or phase lag vs. frequency ($\omega/2\pi$) for several temperatures

from the representative sample with film thickness 1018 nm. Figure 2c displays these data in the form of electrochemomechanical admittance, using frequency as an implicit variable. The electrochemomechanical admittance Y in nm/V is related to the mechanical displacement amplitude A in nm through normalization by the applied bias amplitude E_0 (in Figure 2, E_0 = 128 mV).

Y is defined in equation S1 as the response (displacement D) of the film normalized to the bias signal E, and is characterized by a phase shift φ (equivalent to the negative of the phase lag ϕ) and amplitude A that are both functions of the applied frequency, and are measured as shown in Figure 1c in the text:

$$Y[t] = \frac{D}{E} = \frac{A[\omega]}{E_0}\frac{\sin(\omega t + \varphi[\omega])}{\sin(\omega t)} \quad \text{(S1)}$$

As a complex function of frequency, this can be represented with Equation S2:

$$Y[\omega] = \frac{A[\omega]}{E_0}(\cos\varphi[\omega] + i\sin\varphi[\omega]) \quad \text{(S2)}$$

Figure 2c in the manuscript plots the real and imaginary parts of Equation S2 on the complex plane. Although $|Y|$ is generally normalized by the applied voltage amplitude E_0 (constant for all frequencies in a given condition), this bias normalization factor can be omitted when comparing datasets under constant bias amplitude to indicate the measured mechanical response in units of nm, as is done in the Bode plots in the manuscript.

The following is a discussion of how such a model describes the measured phase lag and amplitude of the mechanical response of the films according to fundamental processes within the material. Figure S3 is a schematic of a similar plot to be used for reference as the relationships between *Y*, *A*, and ϕ are discussed.

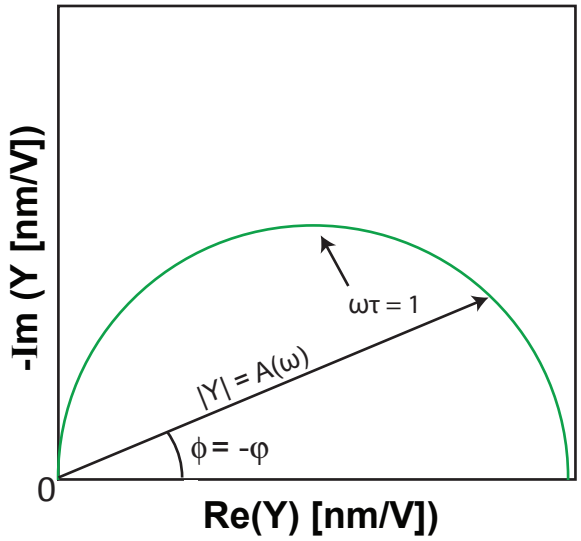

Figure S3. Schematic plot of complex electrochemomechanical admittance *Y*. The x and y axes are the real and imaginary parts of *Y* in nm/V. Each point on the plot can also be represented by its modulus $|Y| = A(\omega)$ (amplitude as a function of frequency) and phase lag ϕ, which is equal to the negative of the phase shift φ (also known as the phase angle). The maximum |Im(*Y*)| in the single semicircle indicates the point at which $\omega\tau = 1$.

To produce the single semi-circle apparent in Figure 2c, the components of *Y* may be modeled using an equivalent circuit with a real component, conductance *G*, and an imaginary component, susceptance *B*, in series. The admittance of these two components is denoted *G'* and $1/i\omega B'$, respectively, giving rise to a total admittance described by equation S3:

$$\bar{Y} = \left(\frac{1}{G} + \frac{1}{B}\right)^{-1} = \frac{G'}{1+(\omega G'B')^2} - \frac{G'i\omega G'B'}{1+(\omega G'B')^2} \quad \text{(S3)}$$

In this representation, $Y = G'$ when $\omega = 0$ (Equilibrium), and $G'B'$ represents a characteristic time constant τ for the response. Therefore, $G' = D_0/E_0$ and $G'B' = \tau$, where D_0 is the equilibrium expansion amplitude for E_0 (a constant across all frequencies), and values for τ are given in the text. With these substitutions, we have Equation S4:

$$\bar{Y} = \frac{D_0/E_0}{1+(\omega\tau)^2} - \frac{(D_0/E_0)i\omega\tau}{1+(\omega\tau)^2} \tag{S4}$$

As shown in the manuscript, it is common to provide the modulus of admittance and phase angle on a Bode plot. The modulus is given by the root of the sum of the squared real and imaginary parts of Y, and the phase angle is equal to the inverse tangent of the ratio of the imaginary and real components as described in the following equations.

$$|Y| = \left(\left(\frac{D_0/E_0}{1+(\omega\tau)^2}\right)^2 + \left(\frac{(D_0/E_0)\omega\tau}{1+(\omega\tau)^2}\right)^2\right)^{1/2} = \frac{D_0/E_0}{\sqrt{1+(\omega\tau)^2}} \tag{S5}$$

$$\varphi(\omega) = \tan^{-1}\left[-\frac{(D_0/E_0)\omega\tau}{D_0/E_0}\right] = \tan^{-1}[-\omega\tau] \tag{S6}$$

Multiplying Equation S5 by the constant applied voltage results in equation S7 used in the manuscript (see Equation 4), and rearranging Equation S6 results in Equation S8, which can be equivalently written as Equation 5 in the manuscript.

$$A(\omega) = \frac{D_0}{\sqrt{(\omega\tau)^2+1}} \tag{S7}$$

$$\varphi(\omega) = -\phi = \tan^{-1}(-\omega\tau) \quad \text{(S8)}$$

$A(\omega)/E_0$ and $\varphi(\omega)$ are the modulus and phase angle, respectively, of Equation S2, confirming that Equation S3 is an equivalent representation of *Y*. These are shown schematically in Figure S3.

With the above equations, D_0 and τ can be derived based on the mechanical measurement of *A* and ϕ and related to the fundamental processes contributing to the measured electromechanical admittance.

Note that as equilibrium is approached ($\omega = 0$), the admittance will be entirely real, and equivalent to $G' = D_0/E_0$. This value gives us information about the total possible mechanical response, and is proportional to the charge storage capacity of the PCO film, given by the chemical capacitance (C_{chem}), as shown by the following proportionality relation:

$$\frac{D_0}{E_0} \propto \frac{\alpha_C \Delta\delta}{E_0} \propto \frac{\Delta q_\delta}{E_0} \propto C_{chem} \quad \text{(S9)}$$

where D_0 is proportional to $\alpha_C \Delta\delta$, the chemical expansion given by Equation 2 in the manuscript, which, in turn, is proportional to the change in number of charges stored as oxygen vacancies, Δq_δ, with C_{chem} being the ratio of stored charge for the given applied voltage.[17]

This correlation also is validated by the fact that charge accumulation in the film determined from I-V data during experiments tracks displacement data with the same phase lag relative to

the applied voltage sinusoids. In Figure 2c, this quantity is also equivalent to the diameter of the semicircle. Since E_0 is a constant (128 mV), an Arrhenius fit such as that shown in Figure 3a in the text to the equilibrium expansion amplitude D_0 gives an activation energy corresponding to that of chemical capacitance in this PCO film. The value measured is 0.53 ± 0.14 eV (standard deviation of 6 measured activation energies), which agrees well with previously reported values for chemical capacitance in PCO and the values reported in this study measured by impedance spectroscopy on these same samples.[18]

Turning to B', when the response of the system is completely out of phase ($\varphi = -\pi/2$) to the applied signal, the complex admittance will be entirely imaginary and equivalent to $B = 1/i\omega B'$, where $B' = \tau/G' = \tau E_0/D_0$. As described earlier, τ is a time constant describing the rate of a process and, following an equivalent circuit representation, can be recast as a resistance multiplied by a capacitance (i.e., RC time constant). As E_0/D_0 is the inverse of C_{chem}, B', from this approach, is equal to a resistance, R (i.e. the resistance to charge passage into the PCO thin film). As described next, this resistance is equivalent to the resistance for ionic transport through the YSZ electrolyte.

As shown schematically in Figure 1b in the text, during these experiments electrical bias V_{WE} is applied between the PCO/Pt working electrode and the reference electrode on the YSZ substrate. Since resistance to oxygen gas exchange at the PCO/Pt electrode is much higher than that of oxygen transport through the YSZ (>100 Ωcm^2 vs. 10 Ωcm^2, respectively at 650^oC), as the PCO film adjusts its vacancy content to match the 'effective pO_2' caused by V_{WE}, oxygen will be pumped primarily through the YSZ electrolyte.[19,20] The rate of adjusting oxygen content in the

PCO film is then limited by diffusion through the YSZ, which will in turn determine the expansion rate. This interpretation is further validated by comparing the activation energy for τ/D_0 (1.05 ± 0.13 eV, see Figure 3a) with the activation energy for ionic conduction in YSZ (~1 eV).[21]

5. Discussion of the influence of a signal collection time delay

This kind of measurement relies on simultaneous collection of signals from the input (driving) signal and the output (displacement) signal. Due to variations in the overall resistance of the conductive pathways providing signals between the signal controller (ModuLab), sample, data acquisition card, and nanoindenter, it is possible for a small additional time delay to appear in the measured phase lag response. This time delay can be modeled in the phase lag frequency response of the system as a second time constant t_d using Equation S10, where the small angle approximation has been applied to the second term:

$$\phi = \tan^{-1}\omega\tau + \tan^{-1}\omega t_d \qquad \text{(S10)}$$

For a representative set of data, consider the $\phi(\omega)$ results shown in Figure 2b for the sample with film thickness 1018 nm at 650°C. Figure S4 displays a comparison of these results when fit to Equation S10 (which estimates τ = 2.4 s and t_d = 0.05 s) vs. Equation 5 (estimating τ = 2.9 s). From this plot, it is apparent that a data collection time delay can account for the additional high frequency phase lag observed for the sample response.

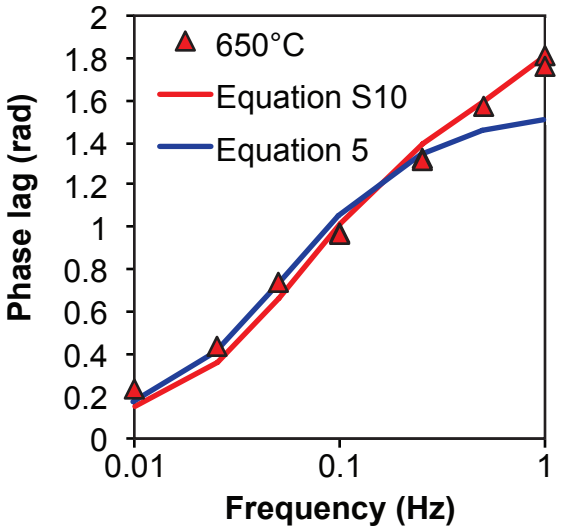

Figure S4. Comparison of fits of the phase lag vs. frequency at 650°C for the sample with film thickness 1018 nm with (Equation S10) and without (Equation 5) inclusion of a signal collection time delay.

Such a time delay would be expected to be consistent for all samples, with very small variations possible depending on the resistance within the Pt connections that link the signal transmission cables to the sample surface. This method of estimating the time delay requires a more complete set of high frequency data points than was generally available for samples in this study. Damping from the pendulum motion of the indenter could also have slightly increased the detected phase lag at high frequencies (on the order of 10 Hz); however the frequencies used in this study are low enough that this is not expected to be a significant contributor to the measured phase lag. Therefore, we focused on a 1st order analysis that most accurately reproduces the combined amplitude and phase lag vs. frequency results with minimal risk of over-fitting.

6. Derivation of chemical strain predictions shown in Figure 3c

Figure 3c shows that the expected out-of-plane equilibrium strain in these PCO films is 0.2 – 0.5% depending on applied bias range and temperature, based on the vacancy concentrations calculated from the defect model of $Pr_{0.1}Ce_{0.9}O_{2-\delta}$ thin films, and accounting for increased out-of-plane deflection resulting from clamping to the substrate.

Figure 3c is derived according to the defect model available in Refs. [20,22] and the chemical expansion coefficient $\alpha_c = 0.087$ reported in Ref. [8]. In this model, the oxide ion vacancy formation reaction is described using Kröger-Vink notation in Equation 1 in the manuscript, reproduced here as Equation S11:

$$2\mathrm{Pr}_{\mathrm{Ce}}^{\times} + \mathrm{O}_{\mathrm{O}}^{\times} \leftrightarrow 2\mathrm{Pr}'_{\mathrm{Ce}} + \mathrm{V}_{\mathrm{O}}^{\cdot\cdot} + \frac{1}{2}\mathrm{O}_2(g) \quad \text{(S11)}$$

Here, $\mathrm{Pr}_{\mathrm{Ce}}^{\times}$ and $\mathrm{Pr}'_{\mathrm{Ce}}$ respectively denote Pr^{+4} and Pr^{+3} on a Ce site, and $\mathrm{O}_{\mathrm{O}}^{\times}$ and $\mathrm{V}_{\mathrm{O}}^{\cdot\cdot}$ respectively denote an oxide ion and an oxide ion vacancy at an oxygen site. Equation S12 describes the equilibrium of this reaction, for which $k^0_{\mathrm{r,Pr}}$ is a pre-exponential term and $\Delta H_{\mathrm{r,Pr}}$ is the enthalpy of reaction:

$$\frac{[Pr'_{Ce}]^2[V_O^{\cdot\cdot}]pO_2^{1/2}}{[Pr_{Ce}^{\times}]^2[O_O^{\times}]} = k^0_{r,Pr}exp\left(\frac{-\Delta H_{r,Pr}}{kT}\right) = K_{r,Pr} \quad \text{(S12)}$$

Enforcing charge neutrality, mass, and site conservation for the composition of $Pr_{0.1}Ce_{0.9}O_{2-\delta}$ after Ref. [20], (and using values of $H_{\mathrm{r,Pr}}$ and k_{r}^0 previously determined from the aforementioned literature), it is possible to determine vacancy concentration expected for this material under the

range of temperatures and effective oxygen partial pressures $pO_{2,eff}$ applied in this study. Effective oxygen partial pressure is determined according to equation S13, following Ref. [20].

$$pO_{2,eff} = pO_{2,g} \exp\left(\frac{4e\Delta E}{kT}\right) \quad \text{(S13)}$$

where $pO_{2,g}$ is the ambient gas pressure, and ΔE is the applied electrical bias. Equation S13 shows that a given applied bias amplitude will give a slightly different effective pO_2 at each temperature, and is used to show the effective pO_2 at 650°C (red curve with dashes and dots) in Figure 3c.

This estimate of expansion includes an approximate twofold increase in the strain of the constrained film as compared to a freestanding membrane. The out-of-plane strain $\varepsilon_{c,z}$ is expected to be larger than the predicted strain $\Delta\varepsilon$ of an unconstrained system under the same conditions by an amount described by Equation S14, where ν is the Poisson's ratio (~0.33 [14]) and σ_0 is a reference stress:[23]

$$\varepsilon_{c,z} = \Delta\varepsilon_c \frac{1+\nu}{1-\nu} - \frac{2\nu\sigma_0}{E} \quad \text{(S14)}$$

To determine predicted chemical strain after assuming a reference stress of 0, Equations 2 in the manuscript and S14 above were combined to form equation S15:

$$\varepsilon_{c,z} = \alpha_c \Delta\delta \frac{1+\nu}{1-\nu} \quad \text{(S15)}$$

Here, ν is the assumed Poisson's ratio of 0.33 and Δδ is the change in vacancy content δ with respect to a sample at the testing temperature and ambient pO_2 at 0 mV bias. Figure 3c shows predicted $\varepsilon_{c,z}$ and Δδ with single curves for each temperature and bias condition because these two factors are proportionally related.

7. Comparison of PCO film breathing to piezoelectric actuation

The electrochemically driven breathing response of these specific non-stoichiometric oxide films presents advantages for high temperature actuation. The predicted strain of these oxides at temperatures above 550°C is ~0.1-0.2% for applied biases of ~0.1 V. Thus, sensors or actuators based on these materials could operate at much lower voltages than a typical high temperature piezoelectric device that requires electric fields on the order of MV/cm to produce strains of the same scale. As an example, we can compare a 1 μm film of a piezoelectric material with strain coefficient d_{11} of 10 pC/N (about the highest currently available for piezoelectrics operating above 400°C [24]) to a PCO/YSZ device with the same film thickness. For the piezoelectric, 100 V of electrical potential are needed to achieve a strain of 0.1%, while for the PCO device, only 100 mV are needed. If both devices are subjected to the same 100 mV, then the achievable actuator 'velocity' (frequency × displacement) will be roughly the same when the piezoelectric is operated at 1 kHz and the PCO device is operated at 1 Hz. Finally, the interfacial stress generated in response to equal applied bias in these devices of comparable size will likewise differ by 3 orders of magnitude if elastic properties are held constant allowing enhanced deflection-based actuation.

8. **Film characterization details**

Figures S5 and S6 show representative film characterization data from atomic force microscopy (AFM) and X-ray diffraction on films of $Pr_{0.1}Ce_{0.9}O_{2-\delta}$ grown by pulsed laser deposition.

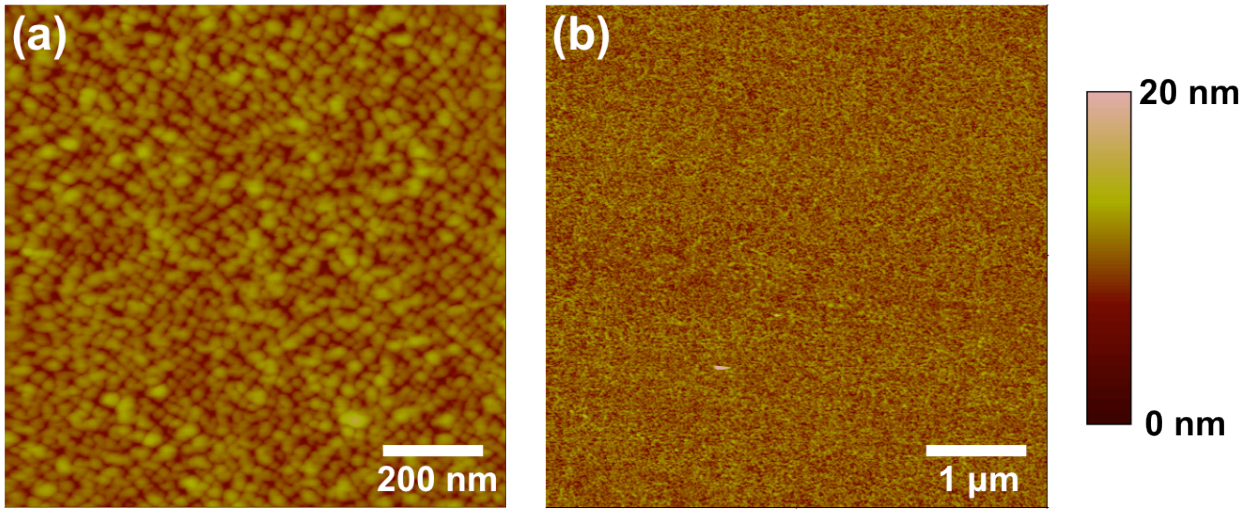

Figure S5. Typical AFM micrograph of as-deposited $Pr_{0.1}Ce_{0.9}O_{2-\delta}$ film surface on a YSZ single crystal substrate for scanned area of 1x1 μm^2 (a) and 5x5 μm^2 (b). Film root mean square surface roughness was generally 1.3 ± 0.2 nm, with grain sizes ranging from 20 – 30 nm.

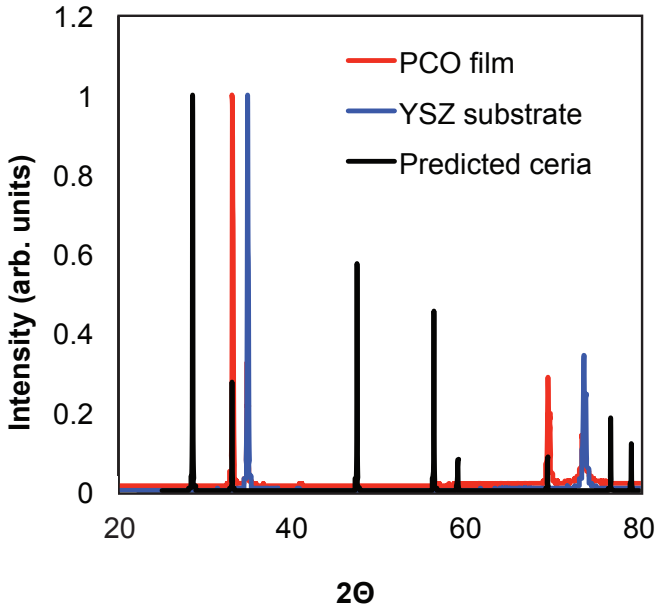

Figure S6. Typical X-ray diffraction patterns for $Pr_{0.1}Ce_{0.9}O_{2-\delta}$ (PCO) thin film and (100) yttria stabilized zirconia (PCO) single crystal substrate as compared to that predicted for undoped cerium oxide. The PCO film pattern confirms (100) crystallographic texture.

9. **Data Processing and Sensitivity Analysis**

Input (driving) and output (displacement) signals were collected by USB-6009 DAQ (National Instruments). The two signals were then each sampled at 20 Hz and a moving average across each driving cycle was subtracted to remove background noise.[25] Each of the two flattened signals was then fitted by linear least squares to a sum of sine and cosine waves (V_{input} = A sin[ωt] + B cos[ωt], V_{output} = C sin[ωt] + D cos[ωt]) where ω is the known driving frequency.[26] The transfer function magnitude and phase lag were calculated according to equations S16 and S17, respectively:

$$A = \frac{\sqrt{(C^2+D^2)}}{\sqrt{(A^2+B^2)}} \tag{S16}$$

$$\phi = \tan^{-1}\frac{B}{A} - \tan^{-1}\frac{D}{C} \tag{S17}$$

The fitting error was calculated according to equation S18:

$$\left(\frac{MSE}{\boldsymbol{D'D}}\right)^{1/2} \tag{S18}$$

where MSE is the mean squared error (the sum of squared residuals divided by the number of degrees of freedom) and **D** is the matrix of partial derivatives of the model evaluated at the final estimates.[25] These errors in A, B, C, and D were propagated with the equations above to determine the errors of the transfer function parameters. At each experimental condition, oscillatory loading (with real-time analysis) was performed until the phase lag converged to

within 0.1 radians and the amplitude to within 0.5 nm, typically 30+ cycles. The values of amplitude and phase lag vs. frequency reported in Figure 2 and used for all data sets to fit to Equations 4 and 5 in the text are the averages of the fitted amplitude and phase lag of the last ten cycles of each measurement, which generally had standard deviations of less than 0.3 nm and 0.1 radians, respectively. In Figure 2, these standard deviations are smaller than the data points. For the slowest frequency measurements (corresponding to the largest measured amplitudes, phase lags nearest to 0, and the most opportunity for mechanical noise and signal drift to affect signal-to-noise ratio), these standard deviations were occasionally larger (<1 nm or 0.2 rad). For replicate measurements performed in the same conditions (temperature, film thickness, applied bias range, etc.) near the centers of the samples, the range of fitted values for D_0 was generally ±3-8%, and for τ was ±2-6%, except in the case of the sample tested for curvature (described in Supplementary Information Section 2), for which the range of τ across a wider lateral spacing range (which could conceivably introduce additional variation) was ±11%.

We show in Figure S7 the result of one of these experiments (650°C, 883 nm film thickness) where the same condition was tested at 3 locations near the sample center. Data points overlap significantly until the highest frequency when some small deviation occurs in the amplitude data. At this point, the amplitude is ~1 nm, which is our stated lower limit of displacement detection. This set of measurements reflects a worst-case scenario in terms of sampling repeatability, and the actual deviations in the resultant calculated values of τ and D_0 from this set of measurements were only 6% and 8%, respectively. Calculated D_0 and τ values are therefore robust to experimental variability, and the error of any reported values can be estimated to be within the ranges reported above.

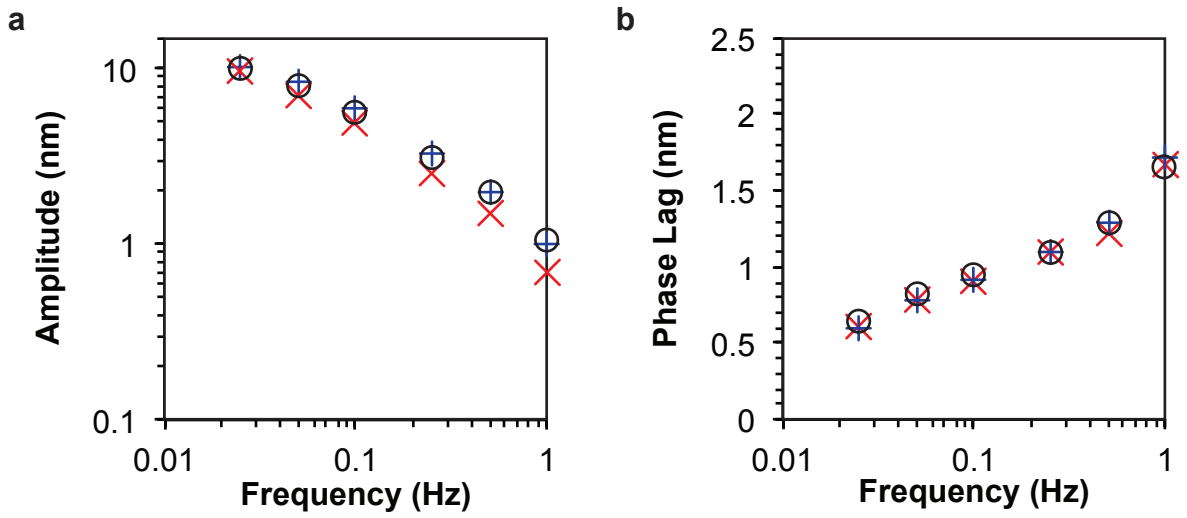

Figure S7. Amplitude (a) and phase lag (b) measured for three replicate experiments near the center of the sample with film thickness 883 nm. Data points overlap significantly up to the highest frequency, when deviation in measured amplitude and phase lag is still less than 1 nm or 0.1 radians.

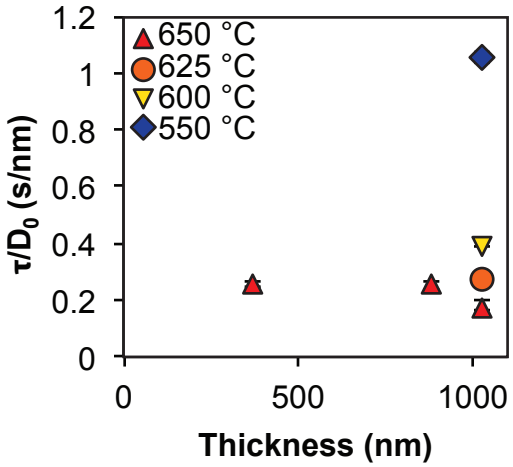

Figure S8. The error in measured inverse deflection rate (τ/D_0) vs. film thickness was small whenever replicate measurements were performed. Error bars denote the range (maximum and minimum) values for each condition.

In fact, the parameters used to fit activation energies were D_0 and τ/D_0. The sample with film thickness 1028 nm was the only one for which multiple positions near the sample center were tested at multiple temperatures, but for those three tests the activation energies of D_0 and τ/D_0

were found to vary by less than 8% and 6%, respectively, displaying minimal sensitivity to experimental variation. Figure S8 shows the variation in τ/D_0 that was observed when assessment was possible; the variability of D_0 alone is reported in Figure 3b in the manuscript.

To consider sample-to-sample variability, we can turn to variation in the quantities that were derived based on data from all samples: activation energies and amplification factor. We report in the text the average and standard deviation for a total of at least 6 measured activation energies across three samples as: -1.05 ± 0.13 eV (for τ/D_0), and 0.53 ± 0.14 eV (for D_0). Thus the sensitivity of the activation energy to experimental and sample-to-sample deviations is on the order of 0.1 eV. For amplification factor (the slope shown in Figure 3d that compares measured displacement D_0 to predicted film thickness change), we applied a bootstrapping algorithm (resampling with replacement) to assess the variation in the linear fit for 1000 bootstrapped samples. Based on this assessment, 95% confidence intervals for the amplification factor and goodness-of-fit parameter R^2 were determined as (4.4, 5.5 nm/nm), and (0.83, 0.98), respectively. Therefore, the sensitivity of the detected amplification factor to sources of variation including but not limited to film thickness measurement error, probe centering error, and sample clamping differences, is on the order of 10%. We also note that the amplification factor is related to the specific substrate thickness (1 mm) and film area (0.64 cm^2) used throughout this work-differing sample geometry would produce a different amplification factor.

10. Stability and precision of the high temperature NanoTest instrument

The NanoTest Vantage instrumented indenter has been designed and demonstrated to enable depth-sensing indentation at temperatures up to 750°C.[13,27,28] All electronics associated with the depth-sensing aspect of the machine are shielded from the high-temperature sample. The root mean square background noise typical of this instrument operated at a temperature of 650°C is 0.2 mV, which is a noise level of 0.4 nm. A detailed description of this high-temperature indentation setup and documentation of its effectiveness for precise measurements at elevated temperature can be found in Refs. [28,29], and here we provide evidence of the stability of the depth-sensing signal when using a frequency-based approach that improves signal-to-noise still further.

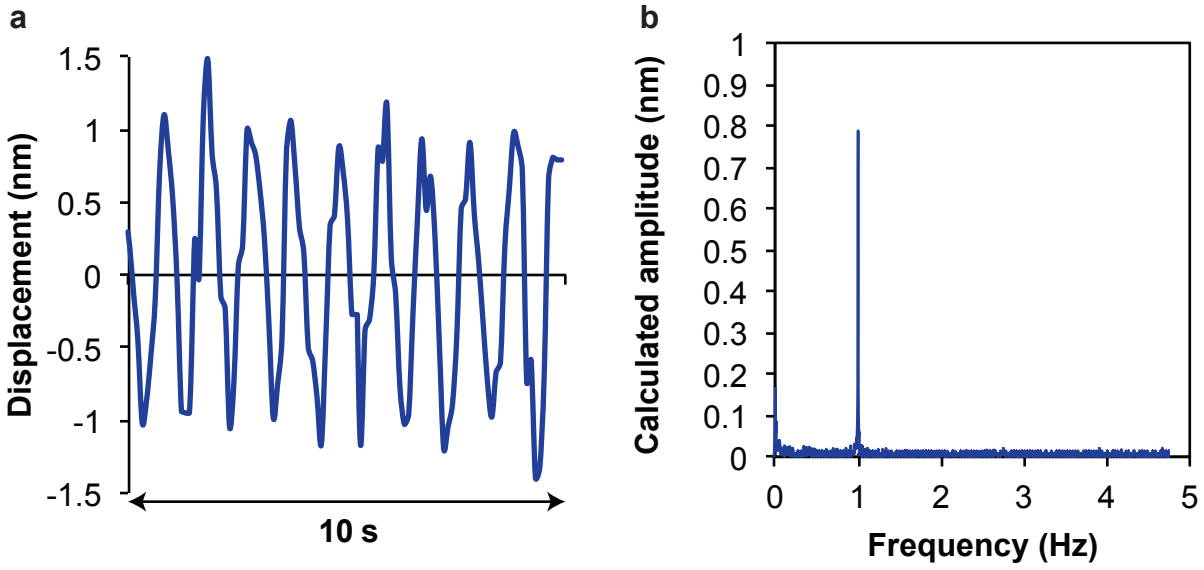

Figure S9. (a) Output of depth-sensing indenter vs. time while in contact with a stage oscillating at 1 Hz with 1 nm amplitude. The probe clearly remains in contact with the oscillating stage. (b) Fast Fourier transform analysis of the depth sensor vs. time over many repeated cycles like those shown in part (a) shows that the 1 Hz frequency is detected.

The NanoTest is sensitive to sub-nm displacements and can easily track oscillations as small as 1 nm at the frequencies used in this study (0.01-1 Hz). To show this, we have documented the output of this kind of machine in contact with an oscillation stage set to run a 1 nm oscillation at a frequency of 1 Hz while in contact with the depth-sensing probe. The output of the depth sensor is plotted vs. time in figure S9a, with a Fourier transform of this signal shown in Figure S9b. The signal was flattened by removing drift after each cycle, and the remaining output clearly shows an amplitude of +/- 1 nm, with the Fourier transform confirming that the 1 Hz frequency is also consistently tracked by the indenter. Given that contact is maintained for this fastest frequency used in this study, the slower frequencies will also maintain probe contact.

The probe material for this study was cubic boron-nitride, which has been used in multiple high temperature indentation studies up to 750°C, including a study of PCO[13,27-29] and is not expected to degrade in air for temperatures below 700°C.[30,31] Starting at about 800°C, a B_2O_3 layer can form that is protective against further oxidation up to 1300°C.[32-34] Although the presence of steam can decrease this temperature to about 900°C[35], this is still well above the temperatures accessed in this study (≤650°C). Furthermore, because the instrumented indenter is being used solely to detect displacements and not to measure mechanical properties, so long as contact is maintained during each test, no particular probe geometry need be maintained.

References

1. Kim, S.-W. & Kim, G.-H. Thickness-profile measurement of transparent thin-film layers by white-light scanning interferometry. *Applied Optics* **38,** 5968–5973 (1999).

2. Sheldon, B. W., Mandowara, S. & Rankin, J. Grain boundary induced compositional stress in nanocrystalline ceria films. *Solid State Ionics* **233,** 38–46 (2013).

3. Hopper, E. M. *et al.* Oxygen exchange in $La_{0.6}Sr_{0.4}Co_{0.2}Fe_{0.8}O_{3-\delta}$ thin-film heterostructures under applied electric potential. *J. Phys. Chem. C* **119,** 19915–19921 (2015).

4. Hiraiwa, C. *et al.* Chemical expansion and change in lattice constant of Y-doped $BaZrO_3$ by hydration/dehydration reaction and final heat-treating temperature. *J Am. Ceram. Soc.* **96,** 879–884 (2013).

5. Grande, T., Tolchard, J. R. & Selbach, S. M. Anisotropic thermal and chemical expansion in Sr-substituted $LaMnO_{3+\delta}$: Implications for chemical strain relaxation. *Chem. Mater.* **24,** 338–345 (2012).

6. Tomkiewicz, A. C., Tamimi, M. A., Huq, A. & McIntosh, S. Evidence for the low oxygen stoichiometry of cubic $Ba_{0.5}Sr_{0.5}Co_{0.5}Fe_{0.5}O_{3-\delta}$ from in-situ neutron diffraction. *Solid State Ionics* **253,** 27–31 (2013).

7. McIntosh, S., Vente, J. F., Haije, W. G., Blank, D. H. A. & Bouwmeester, H. J. M. Oxygen stoichiometry and chemical expansion of $Ba_{0.5}Sr_{0.5}Co_{0.8}Fe_{0.2}O_{3-\delta}$ measured by in situ neutron diffraction. *Chem. Mater.* **18,** 2187–2193 (2006).

8. Bishop, S. R., Tuller, H. L., Kuru, Y. & Yildiz, B. Chemical expansion of nonstoichiometric $Pr_{0.1}Ce_{0.9}O_{2-\delta}$: Correlation with defect equilibrium model. *J. Eur. Ceram. Soc.* **31,** 2351–2356 (2011).

9. Kalinin, S. V. & Balke, N. Local electrochemical functionality in energy storage materials and devices by scanning probe microscopies: Status and perspectives. *Adv. Mater.* **22,** E193–E209 (2010).

10. Kumar, A., Ciucci, F., Morozovska, A. N., Kalinin, S. V. & Jesse, S. Measuring oxygen

reduction/evolution reactions on the nanoscale. *Nature Chem.* **3,** 707–713 (2011).

11. Balke, N. *et al.* Nanoscale mapping of ion diffusion in a lithium-ion battery cathode. *Nature Nanotech.* **5,** 749–754 (2010).

12. Feng, X., Huang, Y.-L. & Rosakis, A. J. On the Stoney formula for a thin film-substrate system with nonuniform substrate thickness. *Transactions of the ASME* **74,** 1276–1281 (2007).

13. Swallow, J. G. *et al.* Operando reduction of elastic modulus in $(Pr,Ce)O_{2-\delta}$ thin films. *Acta Materialia* **105,** 16–24 (2016).

14. Amezawa, K. *et al.* Elastic moduli of $Ce_{0.9}Gd_{0.1}O_{2-\delta}$ at high temperatures under controlled atmospheres. *Solid State Ionics* **198,** 32–38 (2011).

15. Kurosaki, K., Setoyama, D., Matsunaga, J. & Yamanaka, S. Nanoindentation tests for TiO_2, MgO, and YSZ single crystals. *J. Alloys and Compounds* **386,** 261–264 (2005).

16. Kushi, T. *et al.* Elastic modulus and internal friction of SOFC electrolytes at high temperatures under controlled atmospheres. *J. Power Sources* **196,** 7989–7993 (2011).

17. Chen, D., Bishop, S. R. & Tuller, H. L. Non-stoichiometry in oxide thin films: A chemical capacitance study of the praseodymium-cerium oxide system. *Adv. Funct. Mater.* **23,** 2168–2174 (2013).

18. Di Chen. Characterization and control of non-stoichiometry in $Pr_{0.1}Ce_{0.9}O_{2-\delta}$ thin films: Correlation with SOFC electrode performance. (PhD Thesis, Massachusetts Institute of Technology, 2014).

19. Chen, D., Bishop, S. R. & Tuller, H. L. Praseodymium-cerium oxide thin film cathodes: Study of oxygen reduction reaction kinetics. *J. Electroceram.* **28,** 62–69 (2012).

20. Chen, D. & Tuller, H. L. Voltage-controlled nonstoichiometry in oxide thin films:

$Pr_{0.1}Ce_{0.9}O_{2-\delta}$ case study. *Adv. Funct. Mater.* **24,** 7638–7644 (2014).

21. Manning, P. S., Sirman, J. D. & Kilner, J. A. Oxygen self-diffusion and surface exchange studies of oxide electrolytes having the fluorite structure. *Solid State Ionics* **93,** 125–132 (1997).

22. Bishop, S. R., Stefanik, T. S. & Tuller, H. L. Electrical conductivity and defect equilibria of $Pr_{0.1}Ce_{0.9}O_{2-\delta}$. *Phys. Chem. Chem. Phys.* **13,** 10165–10173 (2011).

23. Bishop, S. R. *et al.* Impact of size scale on electro-chemo-mechanical coupling properties in MIECs: Bulk and thin film $(Pr,Ce)O_{2-\delta}$. *ECS Trans.* **61,** 31–36 (2014).

24. Zhang, S. & Yu, F. Piezoelectric materials for high temperature sensors. *J. Am. Ceram. Soc.* **94,** 3153–3170 (2011).

25. Maloney, J. M., Lehnhardt, E., Long, A. F. & Van Vliet, K. J. Mechanical fluidity of fully suspended biological cells. *Biophys. J.* **105,** 1767–1777 (2013).

26. Kutner, M. H., Nachtsheim, C. J., Neter, J. & Li, W. *Applied Linear Statistical Models*. (McGraw-Hill, Boston, 2005).

27. Gibson, J. S. K. L., Roberts, S. G. & Armstrong, D. E. J. High temperature indentation of helium-implanted tungsten. *Materials Science and Engineering A* **625,** 380–384 (2015).

28. Milhans, J. *et al.* Mechanical properties of solid oxide fuel cell glass-ceramic seal at high temperatures. *J. Power Sources* **196,** 5599–5603 (2011).

29. Everitt, N. M., Davies, M. I. & Smith, J. F. High temperature nanoindentation – the importance of isothermal contact. *Philosophical Magazine* **91,** 1221–1244 (2011).

30. Wheeler, J. M. & Michler, J. Indenter materials for high temperature nanoindentation. *Review of Scientific Instruments* **84,** 101301 (2013).

31. Wermer, A. W., ed. *Carbide, Nitride and Boride Materials Synthesis and Processing*.

(Chapman & Hall, 1997).

32. Lavrenko, V. A. & Alexeev, A. F. High-temperature oxidation of boron nitride. *Ceramics International* **12,** 25–31 (1986).

33. Vel, L., Demazeau, G. & Etourneau, J. Cubic boron nitride: synthesis, physicochemical properties and applications. *Materials Science and Engineering* **B10,** 149–164 (1991).

34. Yue, X. Y., Zhang, Y., Wang, J. J., Wang, W. & Ru, H. Q. Surface oxidation behaviour of cubic BN powders. *Key Engineering Materials* **602-603,** 544–547 (2014).

35. Marinescu, I. D., Hitchiner, M. P., Uhlmann, E., Rowe, W. B. & Inasaki, I. *Handbook of Machining with Grinding Wheels*. (CRC Press, Boca Raton, 2015).